Front. Struct. Civ. Eng. 2020, 14(6): 1316–1330
https://doi.org/10.1007/s11709-020-0646-z

TRANSDISCIPLINARY INSIGHT

Deep learning model for estimating the mechanical properties of concrete containing silica fume exposed to high temperatures

Harun TANYILDIZI[a*], Abdulkadir ŞENGÜR[b], Yaman AKBULUT[b], Murat ŞAHİN[a]

[a] *Faculty of Technology, Department of Civil Engineering, Firat University, Elazig 23100, Turkey*

[b] *Faculty of Technology, Department of Electrical-Electronics Engineering, Firat University, Elazig 23100, Turkey*

[*] *Corresponding author. E-mail: htanyildizi@firat.edu.tr*

ABSTRACT In this study, the deep learning models for estimating the mechanical properties of concrete containing silica fume subjected to high temperatures were devised. Silica fume was used at concentrations of 0%, 5%, 10%, and 20%. Cube specimens (100 mm × 100 mm × 100 mm) were prepared for testing the compressive strength and ultrasonic pulse velocity. They were cured at 20°C±2°C in a standard cure for 7, 28, and 90 d. After curing, they were subjected to temperatures of 20°C, 200°C, 400°C, 600°C, and 800°C. Two well-known deep learning approaches, i.e., stacked autoencoders and long short-term memory (LSTM) networks, were used for forecasting the compressive strength and ultrasonic pulse velocity of concrete containing silica fume subjected to high temperatures. The forecasting experiments were carried out using MATLAB deep learning and neural network tools, respectively. Various statistical measures were used to validate the prediction performances of both the approaches. This study found that the LSTM network achieved better results than the stacked autoencoders. In addition, this study found that deep learning, which has a very good prediction ability with little experimental data, was a convenient method for civil engineering.

KEYWORDS concrete, high temperature, strength properties, deep learning, stacked auto-encoders, LSTM network

1 Introduction

Durability is very important for reinforced concrete structures as it affects the service life of these structures. The durability can be affected by sulfate attacks, high-temperature reinforcement corrosion, alkali-aggregate reactions, and the effects of sulfate and carbonation. The effects on the strength properties of concrete subjected to high temperatures have been widely explored [1–6]. Concrete shows better behavior when exposed to fire or high temperatures compared to other construction materials [7]. When concrete is exposed to high temperatures, chemical and physical reactions occur [8], for example, a large loss of compressive strength (CS), wide and deep cracks, disintegrations, and a significant decrease in durability can occur [9–11]. When concrete is exposed to temperatures of 200°C, there are small decreases in strength [12]; however, microcracks were not observed between the cement matrix and ITZ (Interfacial Transition Zone) [13]. The strength of concrete decreases with increasing temperatures. C-S-H starts to deteriorate at 400°C. Moreover, microcracks increase with increasing temperature [12,14–17]. C-H decomposes at 600°C, and aggregate expansion occurs [12,18]. For example, calcareous aggregates disintegrate above this temperature [19], and the damage to the microstructure of the concrete increases [12]. When the temperature reaches 800°C, the strength of the concrete is almost lost [20]; however, the use of pozzolanic materials in concrete increases its resistance to high temperatures. Poon et al. [21] investigated the high-temperature resistance of concrete with silica fume, fly ash, and slag, and found that the use of silica fume with a concentration of more than 5% is not recommended for structures subjected to high temperatures. Furthermore, they found that fly ash and slag are more resistant to high temperatures. Behnood and Ziari

Article history: Received Jul 5, 2019; Accepted Sep 9, 2019

[22] found that a maximum concentration of 6% of silica fume should be used in concretes subjected to high temperatures.

The estimation of the mechanical properties of concrete has been widely explored by scientists [23–30]. However, predicting properties of concrete using deep learning (DL) is very limited in the literature [31–34], while the use of DL has started recently in other engineering applications [35–37]. Cha et al. [31] studied the crack detection of concrete using DL and found it to be the most dependable method for monitoring cracks. Zhang et al. [32] investigated crack detection in asphalt surfaces using DL, and they showed that cracks can be detected with a precision of 90.13%. Deng et al. [34] used DL to determine the CS of recycled concrete, and the prediction results showed that DL yielded a higher precision.

In this study, predictions of the strength properties of concrete containing silica fume subjected to high temperatures were made using DL methods. DL has attracted much attention in image processing and pattern recognition communities, although there are few studies on civil engineering applications. Thus, we opted to use stacked autoencoders and long short-term memory (LSTM) to predict the CS and ultrasonic pulse velocity (UPV) of concrete containing silica fume subjected to high temperatures. Two autoencoder blocks, a hidden layer, and an output layer were used to construct the deep neural networks (DNN) model. A bidirectional LSTM layer, fully connected layer and a regression layer was used to construct the LSTM network. Various experiments were conducted in the MATLAB environment, and the prediction performance was evaluated statistically. The results show that the LSTM network achieves better results compared to the DNN model.

The remainder of this paper was organized as follows. Section 2 introduced the experimental research, and the materials, mixture proportions, curing and heating methods, stacked autoencoders, and LSTM theories were reviewed in this section. Section 3.1 was presented the experimental results. The prediction results using the DNNs and LSTM were discussed in Section 3.2. The paper was concluded in Section 4.

2 Experimental research

2.1 Materials

CEM I/42.5R Portland cement was selected for this study. Olivine (0–3 mm) was selected as the fine aggregate, river sand (3–8 mm) was used as the coarse aggregate, and silica fume was used as a pozzolanic material in this study. The properties of olivine, silica fume, and cement were illustrated in Table 1.

2.2 Mixture proportions

The mixture design was illustrated in Table 2. A superplasticizer was used in this study. The cement dosage was 400 kg/m^3, and the specimens were prepared using a cubic mold with dimensions of 100 mm × 100 mm × 100 mm.

2.3 Curing and heating methods

The specimens were removed from the mold after 24 h. Subsequently, they were cured in water at 20°C±2°C for periods of 7, 28, and 90 d. Following this, they were exposed to temperatures of 200°C, 400°C, 600°C, and 800°C. Each temperature was maintained for 1 h [38]. The heating ratio was set at 2.5°C/min [15,39].

2.4 Stacked auto-encoders

DL has recently demonstrated remarkable performances in classification and forecasting applications [40–44]. In particular, many classification applications have been performed based on convolutional neural networks (CNNs) and LSTM networks [41–43]. In addition, some prediction applications have also been performed using DL. Autoencoders, which have been used for both classification and prediction applications, are one of the DL methods [44]. Autoencoders are unsupervised approaches that use unlabeled data sets as input and transform the input features by minimizing the reconstruction error of the original input features with a single nonlinear hidden-layer neural network. In other words,

Table 1 The chemical properties of cement, olivine, and silica fume

chemical compositions and physical properties	Portland cement	olivine	silica fume
SiO_2 (%)	21.12	42	91.0
Al_2O_3 (%)	5.62	0.5	0.58
Fe_2O_3 (%)	3.24	7	0.24
CaO (%)	62.94	0.05	0.71
MgO (%)	2.73	48	0.33
LOI (%)	1.42	–	1.84
specific surface area (cm^2/g)	3430	–	–
particle size	–	–	< 45 μm (96.5%)
specific gravity (g/cm^3)	3.10	3.3	2.2

Table 2 Mixture proportion of concretes

designation of mixture	cement (kg/m^3)	silica fume (kg/m^3)	*W/C*	super-plasticizer (kg/m^3)	aggregates 0–3 mm (kg/m^3)	aggregates 3–8 mm (kg/m^3)
S0	400	–	0.55	4.8	1259	687
S5	380	20	0.55	4.8	1255	685
S10	360	40	0.55	4.8	1250	682
S20	320	80	0.55	4.8	1239	676

autoencoders can construct the input features exactly by using a complex nonlinear transformation. An illustration of the autoencoder is shown in Fig. 1.

Assuming an input $x \in [0,1]^d$, an autoencoder initially transforms (encoder part) the input x to a hidden feature representation, e.g., $h \in [0,1]^{d'}$, by using the following equation:

$$h = g(Wx + b), \tag{1}$$

where g is a nonlinear activation function, and W and b are the weight matrix and bias vector, respectively. Then, h is retransformed (decoder part) into the reconstructed input feature $\hat{x}$ by the following equation:

$$\hat{x} = g(W'h + b'), \tag{2}$$

where W' and b' are the reconstruction parameters. The parameters, which are defined in Eqs. (1) and (2), are determined by minimizing the average reconstruction error.

Final DNNs can be obtained by stacking the auto-encoders, as shown in Fig. 1. The encoder block contains a structure, as shown in Fig. 2.

In the training of DNNs, the autoencoder is initially employed to minimize the reconstruction error of the input data. The output of the autoencoder is given to the hidden unit, and the hidden unit is connected to the output layer. As mentioned earlier, the auto-encoders work in an unsupervised fashion; however, the stacked AEs are trained with backpropagation on the entire network to fine-tune the weights and biases in a supervised manner.

2.5 LSTM

The LSTM network is a type of recurrent neural network (RNN). It contains three types of layers: input, hidden recurrent, and output layers, as shown in Fig. 3 [41–43]. The memory block, which is a new structure, is the difference between the LSTM and RNN models. The memory block consists of four main elements: the input gate, memory cell, forget gate, and output gate. The memory-cell element contains a self-recurrent connection. Gates in the memory cells that change the state of the signal while allowing or blocking the output gate prevent the memory-cell state from having an effect on the rest of the network. The forget gate allows the memory cell to forget its previous state when the information stream is out of date. As seen in Fig. 3, the weighted "peephole" connections from the cell to the gates are shown by dashed lines.

The self-recurrent connection has a weight of 1.0 and ensures that the state of a memory cell that prevents any

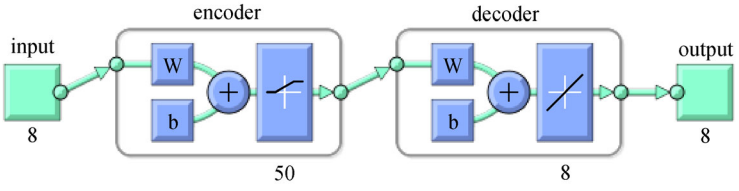

Fig. 1 An illustration for auto-encoder.

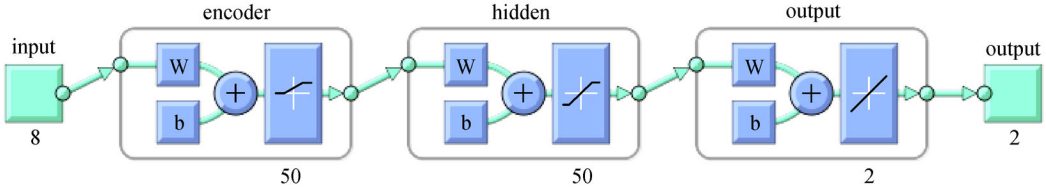

Fig. 2 The illustration of the whole DNNs structure.

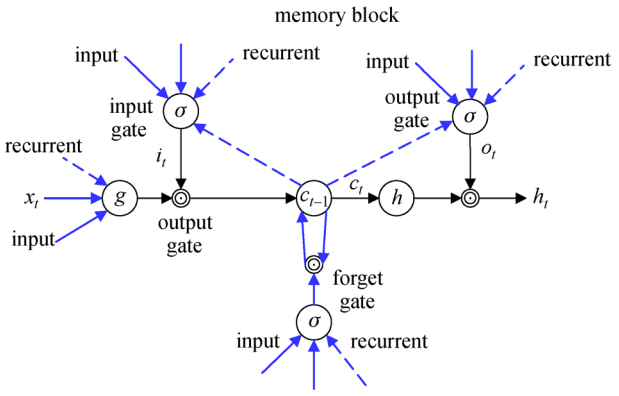

Fig. 3 The structure of the LSTM unit.

external interference remains constant from one time phase to another. The following equations explain how a memory block works in each t step:

$$i_t = \sigma(W_i x_t + U_i h_{t-1} + b_i), \tag{3}$$

$$f_t = \sigma(W_f x_t + U_f h_{t-1} + b_f), \tag{4}$$

$$c_t = f_t \cdot c_{t-1} + i_t \cdot g(W_c x_t + U_c h_{t-1} + b_c), \tag{5}$$

$$o_t = \sigma(W_o x_t + U_o h_{t-1} + V_o c_t + b_o), \tag{6}$$

$$h_t = o_t \cdot h(c_t), \tag{7}$$

where W_i, W_f, W_c, W_o, U_i, U_f, U_c, U_o, and V_o are the weight matrices, and b_i, b_f, b_c, and b_o are bias vectors. i_t, f_t, and o_t are the activations for the input, forget, and output gates, respectively. While c_t shows the state of the memory cell at time t, h_t indicates the output of the memory cell at time instant t. The gate activation function $\sigma(x)$ is assigned as the standard logistics sigmoid function. $g(x)$ and $h(x)$ are defined as the input and output activations, and the 'tanh' function is used for both $g(x)$ and $h(x)$.

3 Results

3.1 Experimental results

The concretes with silica fume were subjected to high temperatures in this study. For this purpose, cubic samples were prepared for UPV and CS tests. The samples were cured in water at 20°C±2°C for periods of 7, 28, and 90 d. Then, they were exposed to temperatures of 200, 400, 600, and 800°C. The CS results of samples exposed to high temperatures were depicted in Figs. 4–6.

The CSs of concrete exposed to a temperature of 20°C were 23.8, 28.09, 25.13, and 23.41 MPa for silica fume contents of 0%, 5%, 10%, and 20% for a period of 7 d, respectively. The CSs of concrete exposed to a temperature of 200°C were 23.5, 27.5, 24.57, and 21.88 MPa for 0%, 5%, 10%, and 20% for a period of 7 d, respectively. The CSs of concrete exposed to a temperature of 400°C were 18.97, 19.8, 19.47, and 18.56 MPa for 0%, 5%, 10%, and 20% for a period of 7 d, respectively. The CSs of concrete exposed to a temperature of 600°C were 12.54, 14.97, 13.04, and 12.44 MPa for 0%, 5%, 10%, and 20% for a period of 7 d, respectively. The CSs of concrete exposed to a temperature of 800°C were 6.71, 8.21, 7.02, and 5.82 MPa for 0%, 5%, 10%, and 20% for a period of 7 d, respectively.

The CSs of concrete exposed to a temperature of 20°C were 30.22, 34.15, 31.85, and 29.57 MPa for silica fume contents of 0%, 5%, 10%, and 20% at 28 d, respectively. The CSs of concrete exposed to a temperature of 200°C were 30.05, 32.52, 31.32, and 28.82 MPa for 0%, 5%, 10%, and 20% at 28 d, respectively. The CSs of concrete exposed to a temperature of 400°C were 20.56, 21.91, 21.03, and 19.64 MPa for 0%, 5%, 10%, and 20% at 28 d, respectively. The CSs of concrete exposed to a temperature of 600°C were 17.3, 20.09, 18.09, and 16.01 MPa for 0%, 5%, 10%, and 20% at 28 d, respectively. The CSs of concrete exposed to a temperature of 800°C were 8.21,

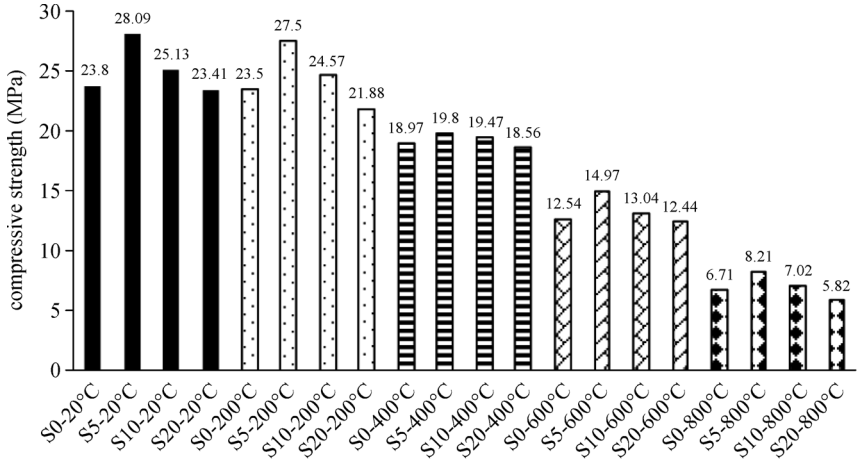

Fig. 4 CS results at 7 d.

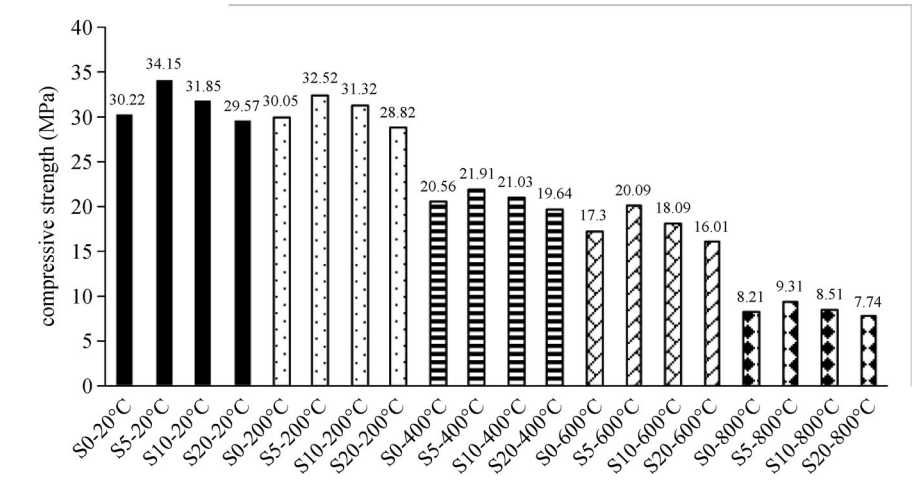

Fig. 5 CS results at 28 d.

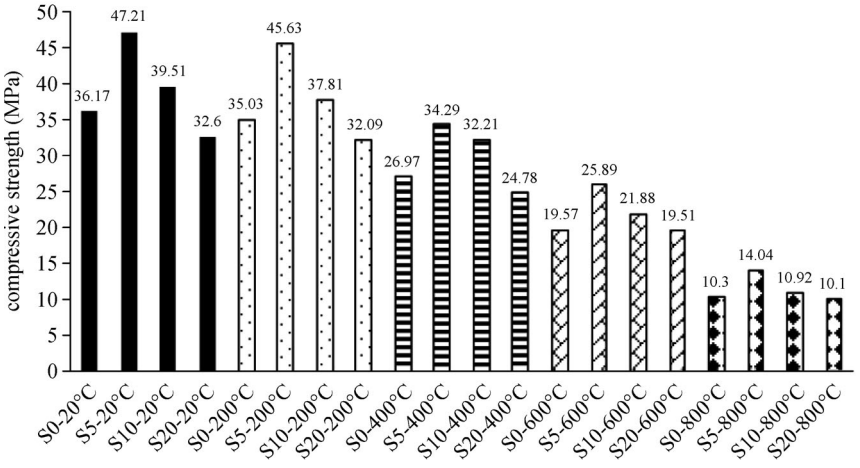

Fig. 6 CS results at 90 d.

9.31, 8.51, and 7.74 MPa for 0%, 5%, 10%, and 20% at 28 d, respectively.

The CSs of concrete exposed to a temperature of 20°C were 36.17, 47.21, 39.51, and 32.6 MPa for silica fume contents of 0%, 5%, 10%, and 20% at 90 d, respectively. The CSs of concrete exposed to a temperature of 200°C were 35.03, 45.63, 37.81, and 32.09 MPa for 0%, 5%, 10%, and 20% at 90 d, respectively. The CSs of concrete exposed to a temperature of 400°C were 26.97, 34.29, 32.21, and 24.78 MPa for 0%, 5%, 10%, and 20% at 90 d, respectively. The CSs of concrete exposed to a temperature of 600°C were 19.57, 25.89, 21.88, and 19.51 MPa for 0%, 5%, 10%, and 20% at 90 d, respectively. The CSs of concrete exposed to a temperature of 800°C were 10.3, 14.04, 10.92, and 10.1 MPa for 0%, 5%, 10%, and 20% at 90 d, respectively.

It can be observed from Figs. 4–6 that the highest CS for all the curing days was determined for the concretes including 5% silica fume. Based on the reference concretes at 20°C, 200°C, 400°C, 600°C, and 800°C in Fig. 4, the increases in the CSs of concrete including 5% silica fume at the same temperatures were 18.02%, 17.02%, 4.38%, 19.38%, and 22.35%, respectively. Based on the reference concretes at 20°C, 200°C, 400°C, 600°C, and 800°C in Fig. 5, the increases in the CSs of concrete including 5% silica fume at the same temperatures were found to be 13%, 8.22%, 6.57%, 16.13%, and 13.40%, respectively. Based on the reference concretes at 20°C, 200°C, 400°C, 600°C, and 800°C in Fig. 6, the increases in the CS of concrete including 5% silica fume at the same temperatures were 30.52%, 30.26%, 27.14%, 32.29%, and 36.31%, respectively. According to the literature, a concentration of more

than 6% silica fume should not be used in concrete exposed to high temperatures [21,22]. Similar results were obtained in this study. The samples containing 5% silica fume were found to be the samples with the highest resistance to high temperature in this study. The UPV are shown in Figs. 7–9.

It can be seen from Figs. 7–9 that the highest UPV was found for concretes with 5% silica fume for all numbers of curing days. Based on the reference concretes at 20°C, 200°C, 400°C, 600°C, and 800°C in Fig. 7, the increases in the UPVs of concrete including 5% silica fume at the same temperatures were found to be 3.46%, 7.59%, 7.70%, 6.62%, and 4.90%, respectively. Based on the reference concretes at 20°C, 200°C, 400°C, 600°C, and 800°C in Fig. 8, the increases in the UPVs of concrete including 5% silica fume at the same temperatures were found to be 7.76%, 10.51%, 8.7%, 10%, and 7.58%, respectively. Based on the reference concretes at 20°C, 200°C, 400°C, 600°C, and 800°C in Fig. 9, the increases in UPVs of concrete including 5% silica fume at the same temperatures were found to be 9.22%, 9.22%, 6.17%, 2.36%, and 10.33%, respectively. High-temperature cracking causes vapor pressure in the pores and a thermal gradient in the concrete [20]. These two effects cause the concrete to crack and disintegrate. Therefore, the CS and UPV will decrease with the increase in temperature due to the increases in the gap. The use of silica fume is known to increase the strength properties of concrete; however, the use of silica fume in concrete exposed to high temperatures can reduce the high-temperature resistance of the concrete. Many studies have found that more than 6% silica fume should not be used [21,22]. In this study, concretes with 5% silica fume were found to be high in both the UPV and CS at all temperatures and curing times. However, in concrete with 10% silica fume, a higher strength than the reference sample was obtained at all curing times and temperatures. Xie et al. [45] reported that the best concentration of silica fume was found to be 4% for concrete exposed to

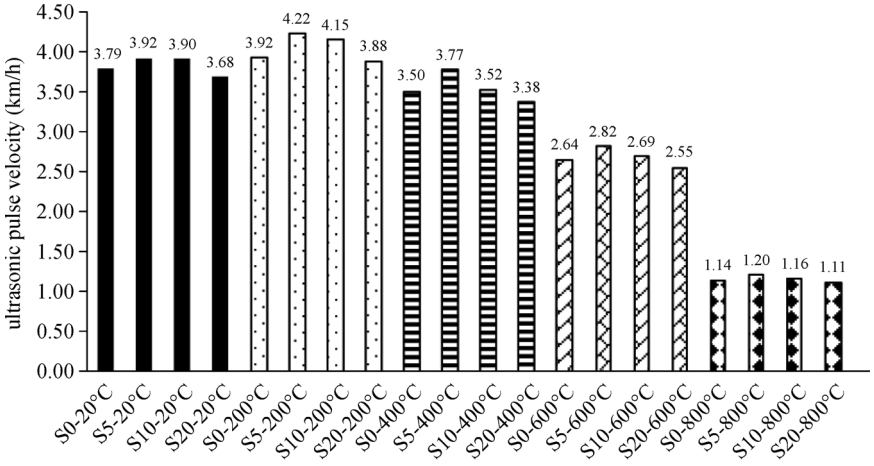

Fig. 7 UPV results at 7 d.

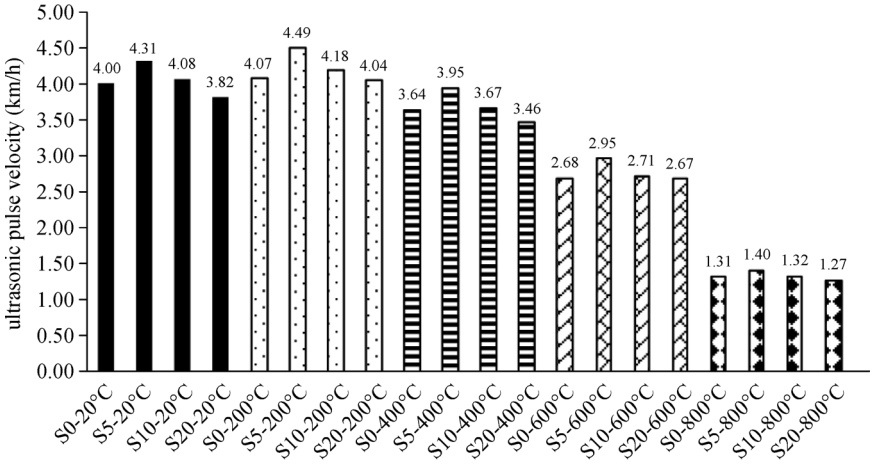

Fig. 8 UPV results at 28 d.

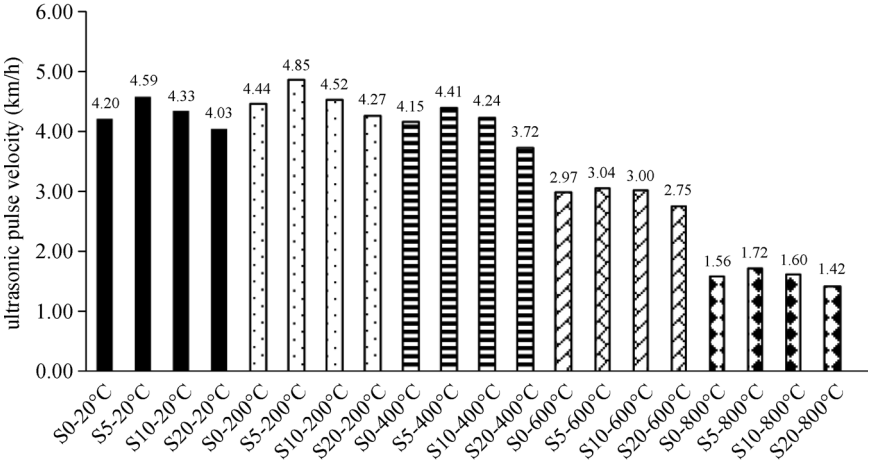

Fig. 9 UPV results at 90 d.

temperatures over 400°C. They said that this was due to the pozzolanic effect.

3.2 Deep-learning-based forecasting results

3.2.1 DNN model results

In this section, a DNN model was devised to estimate the CSs and UPVs of concrete containing silica fume exposed to high temperatures. A data set consisting of 48 samples was used in the DNN model. There were eight inputs in the DNN model. These were determined as cement, silica fume, water/cement, super-plasticizer, 0–3 mm aggregates, 3–8 mm aggregates, curing, and temperature. There were used two outputs as CS and UPV in the DNN model. A zero-mean-unit-variance normalization was applied to the data set. All coding was carried out in the MATLAB neural network and DL toolboxes.

The DNN model used in the experiments was shown in Fig. 10. Two autoencoder blocks, a hidden layer, and an output layer were used to construct the DNN model. Each autoencoder block contained 50 hidden neurons. The 'L2WeightRegularization' parameter was set to 0.001; the 'SparsityRegularization' parameter was chosen to be 4; the 'SparsityProportion' parameter was assigned to be 0.05; and the 'DecoderTransferFunction' was selected as 'purelin'. The hidden layer also contained 50 neurons. The Levenberg-Marquardt backpropagation algorithm was used to train the DNNs. Four different evaluation metrics were used in the performance evaluation of the proposed method: the mean square error (*MSE*), peak signal-to-noise ratio (*PSNR*), *R* value, and mean absolute percentage error (*MAPE*) [46,47]. A lower *MSE*, higher *PSNR*, R^2 close 1, and lower *MAPE* scores indicate a good performance. Three different training and testing sets were used in the experiments. In the first experiment, a randomly-selected 60% of the data set was used to training in the DNN, and the remaining 40% was used for testing. In the second experiment, a randomly-selected 70% of the data set was used for training in the DNN, and 30% of the data was used for testing. In the last experiment, 80% of the data set was used for training, and the remaining 20% of the data was used for testing in the DNN. The evaluation metric results obtained for the CS predictions of DNN were given in Table 3. The columns in Table 3 shown the experiments, and the rows shown the evaluation metrics for the CS prediction. The evaluation metrics in the first experiment (60-40) were obtained as 0.0713 (*MSE*), 59.5991 (*PSNR*), 0.9349 (*R*-value), and 10.7343 (*MAPE*) scores. The evaluation metrics in the second experiment (70-30) were found as 0.0417 (*MSE*), 61.9296 (*PSNR*), 0.9561 (*R*-value), and 0.1052 (*MAPE*). Finally, the evaluation metrics in the third experiment (80-20) were obtained as 0.0322 (*MSE*), 63.0554 (*PSNR*), 0.9565 (*R*-value), and 3.8593 (*MAPE*) scores. As observed in Table 3, the third experiment (80-20) yielded better scores than did the first (60-40) and second (70-30) experiments. In addition, the second experiment produced better results than did the first experiment. In addition, the actual and predicted results were plotted in Fig. 11. The red color and the blue color in Fig. 11 shown the actual results and the predicted results, respectively. As shown in Fig. 11, the best fit was obtained from the third experiment. Moreover, successful fits were also obtained from the other experiments. Table 4 shown the performances of the predictions of the DNN model for the UPV. As seen in Table 4, the lowest *MSE* (0.0110) and *MAPE* (5.8039) and the highest *PSNR* (75.0843) and *R*-value (0.9842) scores were obtained in the third experiment. This means that the third experiment outperformed the first and second experiments. In addition, the performance scores of the second experiment were better than those of the first experiment. Figure 12 shown the predicted and actual results of the UPVs for all experiments. The first column of Fig. 12 illustrated the first experiment. The second and third columns shown the predicted and actual results for the second and third

experiments, respectively. As seen in Fig. 12, the best fit was obtained from the third column. Furthermore, Figs. 13 and 14 shown the regression plots obtained for the DNN-based predicted and actual results for the CS and UPV. The highest R square value for the CS and UPV was obtained as 0.9565 and 0.9842 in the third experiment, respectively. Because the best performance was obtained in the third experiment, the training and testing processes of the DNNs model for the CS and UPV were given for the third experiment (80-20) in Figs. 15 and 16.

3.2.2 LSTM network model results

In this section, the LSTM network model was used to forecast the CSs and UPVs of concrete with silica fume subjected to high temperatures. The same data set used in the DNN model was also used in this section. The parameters of the LSTM were determined heuristically while running the experiments. The input sequence size of the LSTM was set to 8. A zero mean and unit-variance normalization were applied to the input data. A bidirectional LSTM layer with an output size of 250 was used. The fully connected layer of the LSTM network was set to 1, and a regression layer was used following the fully connected layer. The 'adam' solver was chosen as the LSTM training method. The gradient threshold of the LSTM network was set to 1. The mini-batch size of the LSTM network was 200. The initial learning rate of the LSTM network was chosen to be 0.01. The learning rate was decreased with a dropped factor of 0.001 during the

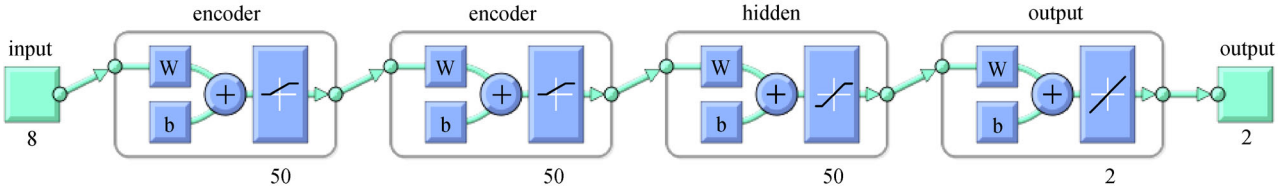

Fig. 10 The DNNs model that was used in experiments.

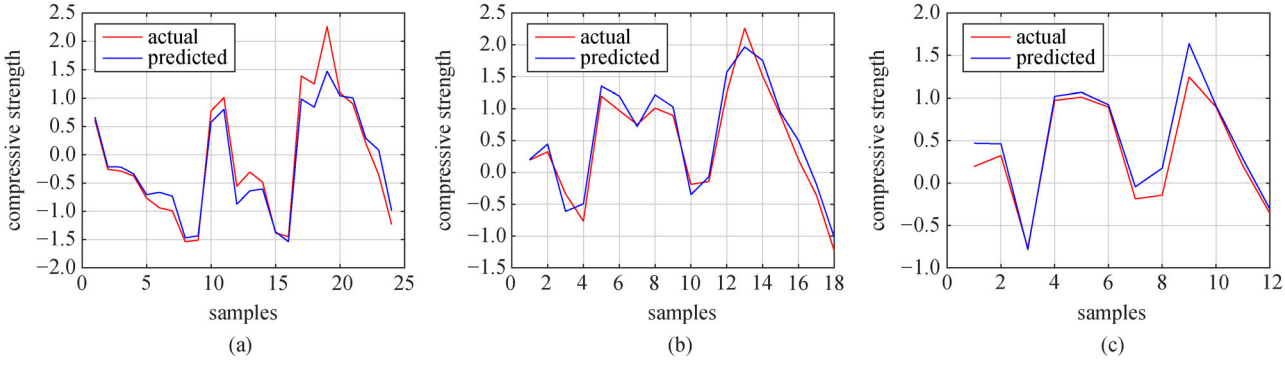

Fig. 11 Illustration of the DNN-based predicted and actual results for CS. (a) First experiment (60-40); (b) second experiment (70-30); (c) third experiment (80-20).

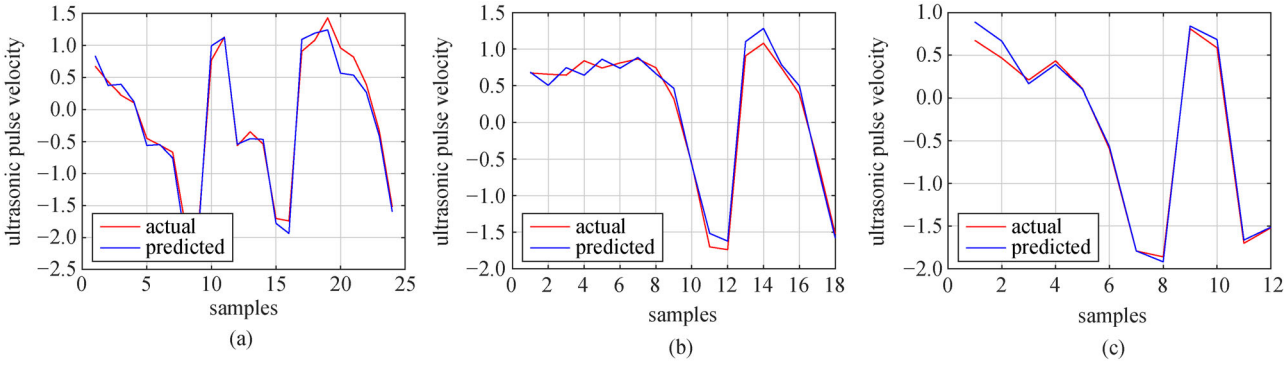

Fig. 12 Illustration of the DNN-based predicted and actual results for UPV. (a) First experiment (60-40); (b) second experiment (70-30); (c) third experiment (80-20).

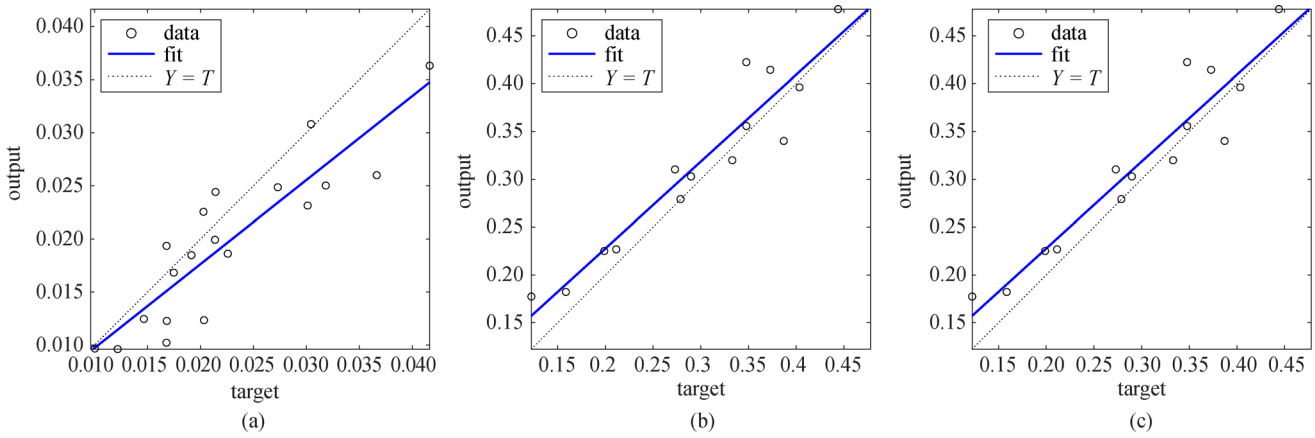

Fig. 13 The regression plots for the DNN-based predicted and actual results of CS. (a) First experiment (60-40); (b) second experiment (70-30); (c) third experiment (80-20).

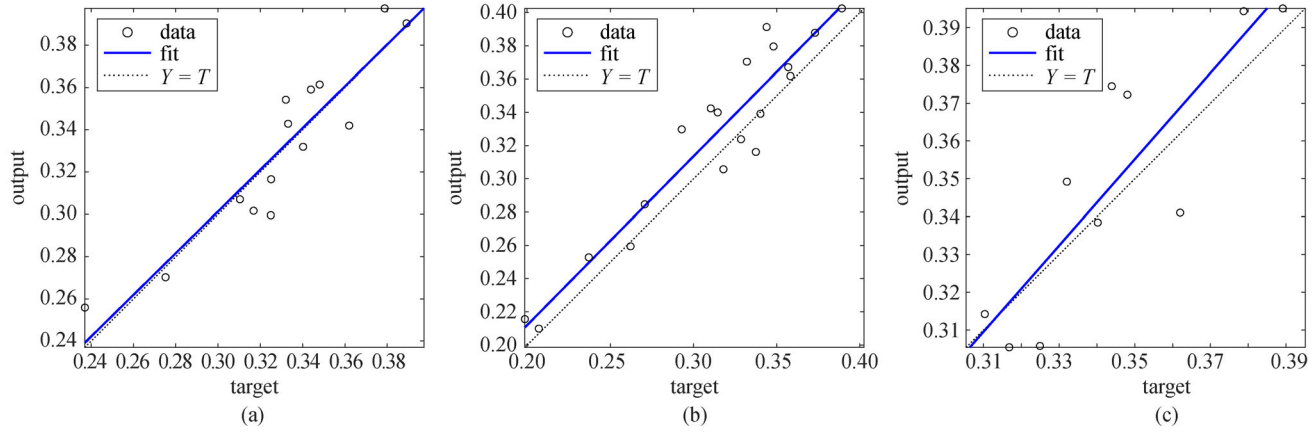

Fig. 14 The regression plots for the DNN-based predicted and actual results of UPV. (a) First experiment (60-40); (b) second experiment (70-30); (c) third experiment (80-20).

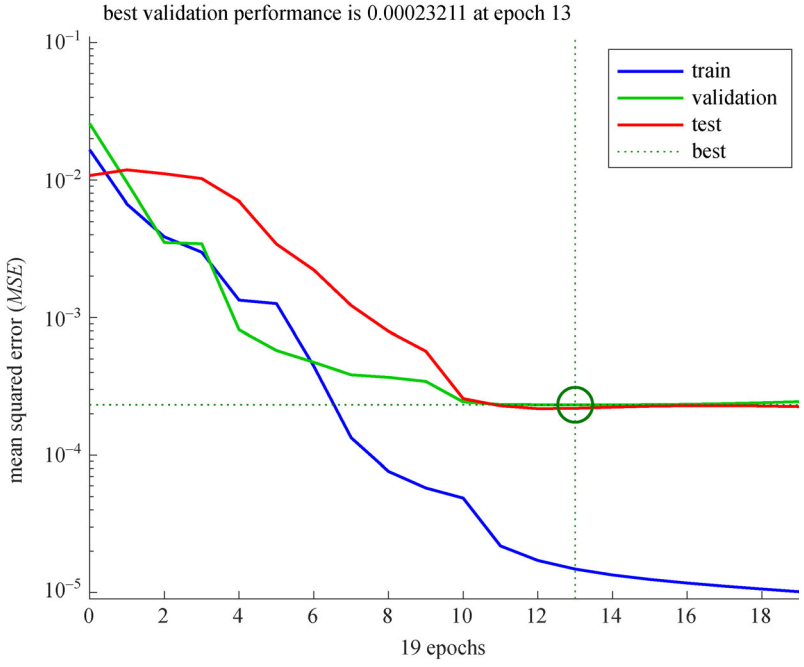

Fig. 15 The training and testing processes of the DNN model for CS.

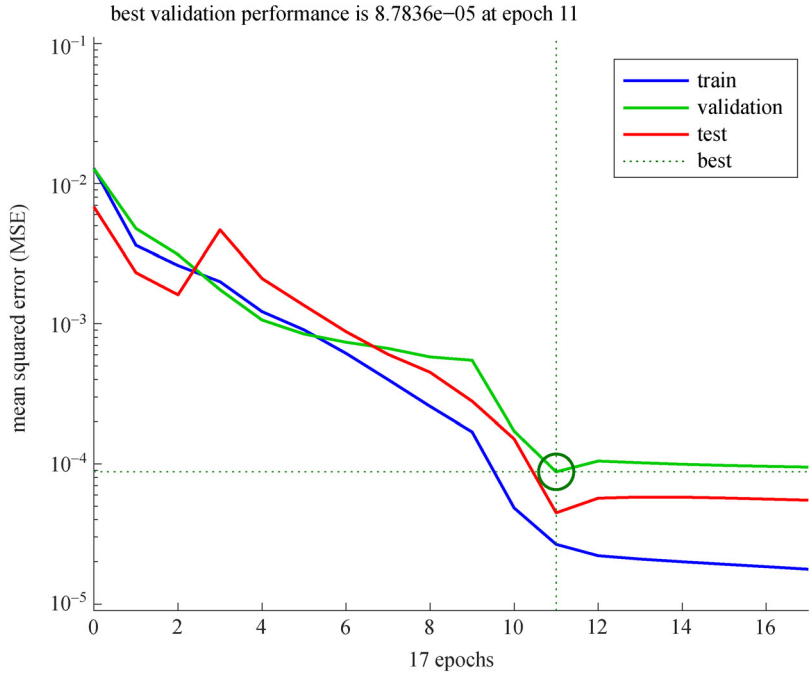

Fig. 16 The training and testing processes of the DNN model for UPV.

Table 3 DNN-based prediction evaluation metrics for CS

item	first experiment (60-40)	second experiment (70-30)	third experiment (80-20)
MSE	0.0713	0.0417	0.0322
PSNR	59.5991	61.9296	63.0554
R-value	0.9349	0.9561	0.9565
MAPE	10.7343	4.1052	3.8593

Table 4 DNN-based prediction evaluation metrics for UPV

item	first experiment (60-40)	second experiment (70-30)	third experiment (80-20)
MSE	0.0250	0.0149	0.0110
PSNR	64.1514	66.4000	75.0843
R-value	0.9761	0.9834	0.9842
MAPE	7.4453	6.0586	5.8039

training with 100 epoch periods. The evaluation metric results obtained for the CS predictions of the LSTM model were given in Table 5. As seen in Table 5, the evaluation metrics for the first experiment (60-40) were 0.0620 (*MSE*), 59.2055 (*PSNR*), 0.9332 (*R*-value), and 10.4899 (*MAPE*) scores. In the second experiment (70-30), the evaluation metrics were obtained as 0.0418 (*MSE*), 61.9193 (*PSNR*), 0.9319 (*R*-value), and 9.0691 (*MAPE*) scores. Finally, the evaluation metrics for the third experiment (80-20) were found as 0.0288 (*MSE*), 63.5427 (*PSNR*), 0.9760 (*R*-value), and 8.7020 (*MAPE*) scores. As observed in Table 5, the third experiment (80-20) yielded better scores than did the first (60-40) and second (70-30) experiments. In addition, the second experiment produced better results than did the first experiment. Figure 17 shown the LSTM-based predicted and actual results of the CSs for all experiments. The first column of Fig. 17 illustrated the results of the first experiment. The second and third columns shown the predicted and actual results for the second and third experiments, respectively. As seen in Fig. 17, the best fit was obtained for the third column. The LSTM-based prediction scores for the UPVs were given in Table 6. Similar to the previous results, the best performance was obtained for the third experiment. In addition, the second experiment produced better evaluation scores than did the

first experiment. Figure 18 also shown the LSTM-based predicted and actual results of the UPVs for all experiments. The first column of Fig. 18 illustrated the results for the first experiment. The second and third columns shown the predicted and actual results for the second and third experiments, respectively. As seen in Fig. 18, the best fit was obtained for the third column. Figures 19 and 20 shown the regression plots obtained for LSTM-based predicted and actual results for the CS and UPV. The highest R square value for the CS and UPV was found as 0.9760 and 0.9924 in the third experiment, respectively. In Fig. 21 and 22, the training and testing processes of the LSTM model for the CS and UPV were given for the 80-20 training-testing rates. Since the best performance was obtained in 80-20 rate, the training and testing processes of this rate was given. The comparison of the computational times of the DNN and LSTM for both the CS and UPV predictions were tabulated in Table 7. As seen in Table 7, the DNNs computation time was obtained less than the LSTM computation time for all predictions.

4 Conclusions

In this study, DL models were devised to predict the CS and UPV of concrete containing silica fume subjected to high temperatures. For this purpose, the stacked auto-encoders and LSTM networks, which were well known DL

Table 5 LSTM-based prediction evaluation metrics for CS

item	first experiment (60-40)	second experiment (70-30)	third experiment (80-20)
MSE	0.0620	0.0418	0.0288
PSNR	59.2055	61.9193	63.5427
R-value	0.9332	0.9319	0.9760
MAPE	10.4899	9.0691	8.7020

Table 6 LSTM-based prediction evaluation metrics for UPV

item	first experiment (60-40)	second experiment (70-30)	third experiment (80-20)
MSE	0.0155	0.0117	0.0109
PSNR	66.2263	67.8183	69.6375
R-value	0.9797	0.9889	0.9924
MAPE	8.6751	8.4446	8.1583

Table 7 The comparison of computational times of DNN and LSTM

item	the computational times (s)	
	DNN	LSTM
CS (third experiment)	54.23 (19 Epochs)	334 (800 Epochs)
UPV (third experiment)	51.12 (17 Epochs)	341 (800 Epochs)

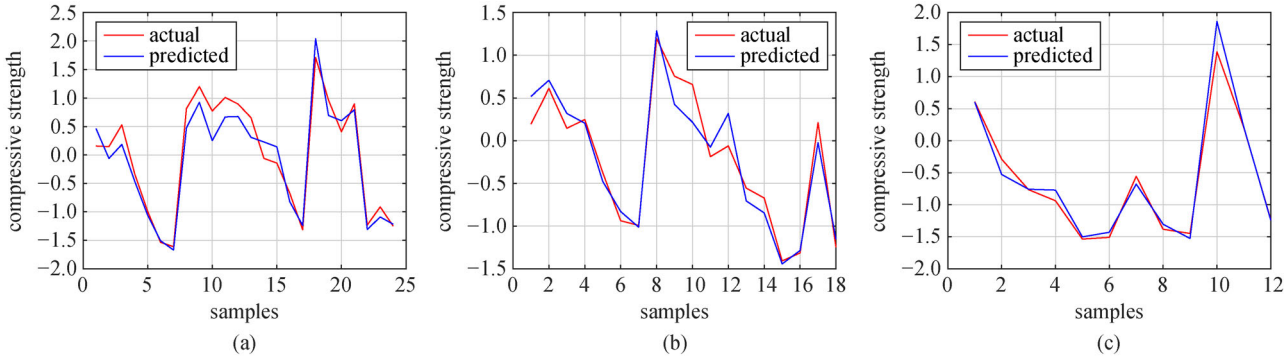

Fig. 17 Illustration of the LSTM-based predicted and actual results of CS. (a) First experiment (60-40); (b) second experiment (70-30); (c) third experiment (80-20).

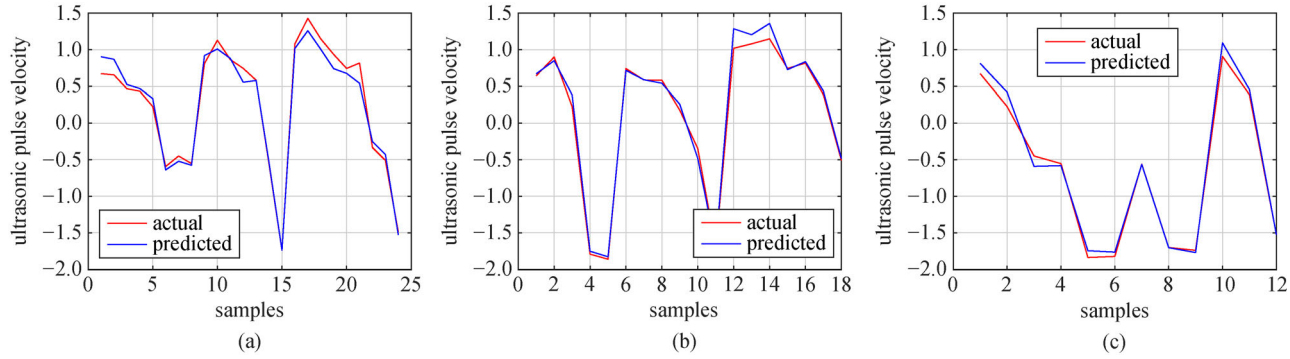

Fig. 18 Illustration of the LSTM-based predicted and actual results of UPV. (a) First experiment (60-40); (b) second experiment (70-30); (c) third experiment (80-20).

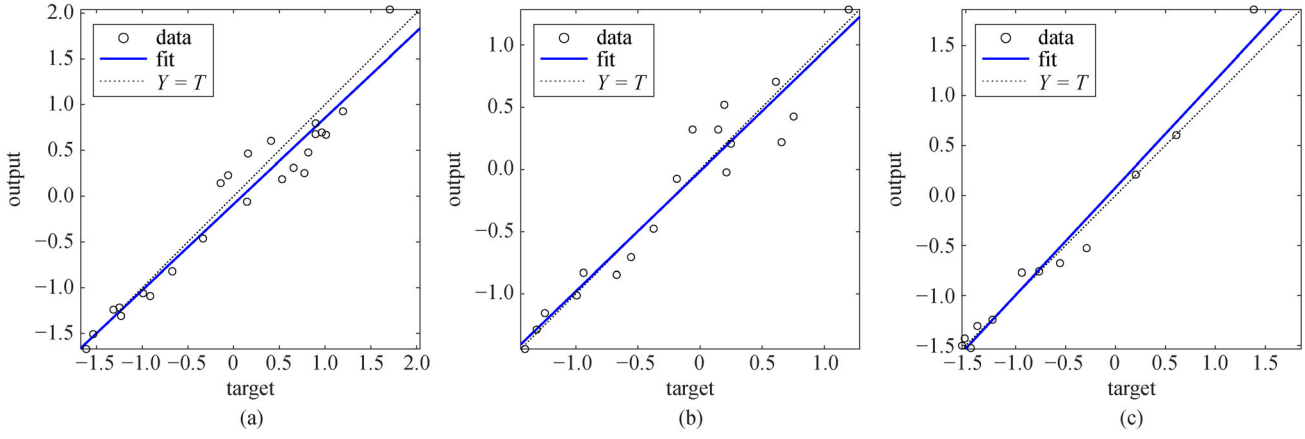

Fig. 19 The regression plots for the LSTM-based predicted and actual results for CS. (a) First experiment (60-40); (b) second experiment (70-30); (c) third experiment (80-20).

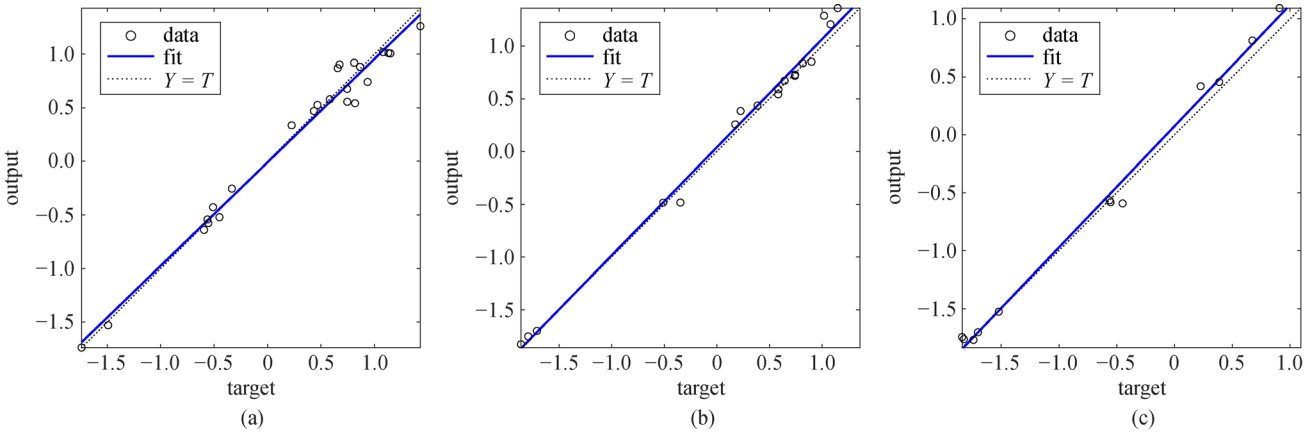

Fig. 20 The regression plots for the LSTM-based predicted and actual results for UPV. (a) First experiment (60-40); (b) second experiment (70-30); (c) third experiment (80-20).

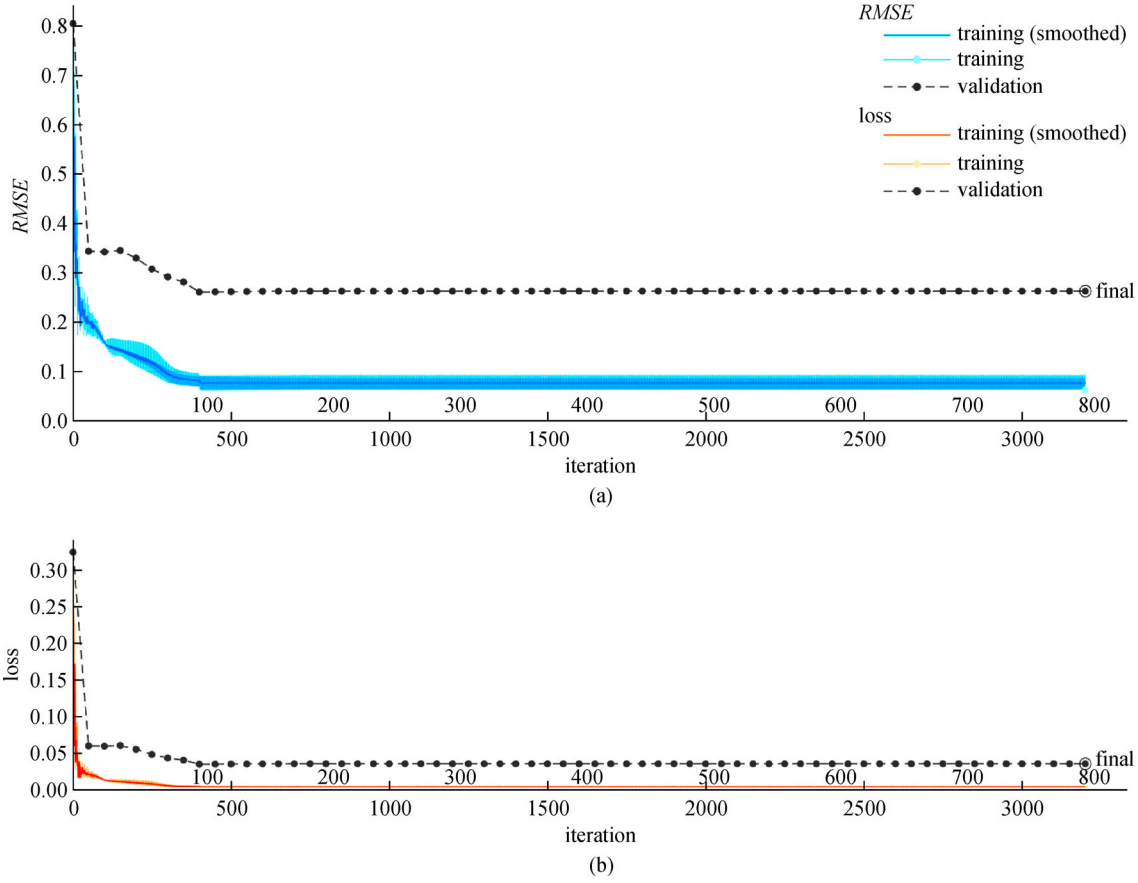

Fig. 21 The training and testing processes of the LSTM network model (third experiment) for CS. (a) *RMSE*; (b) loss.

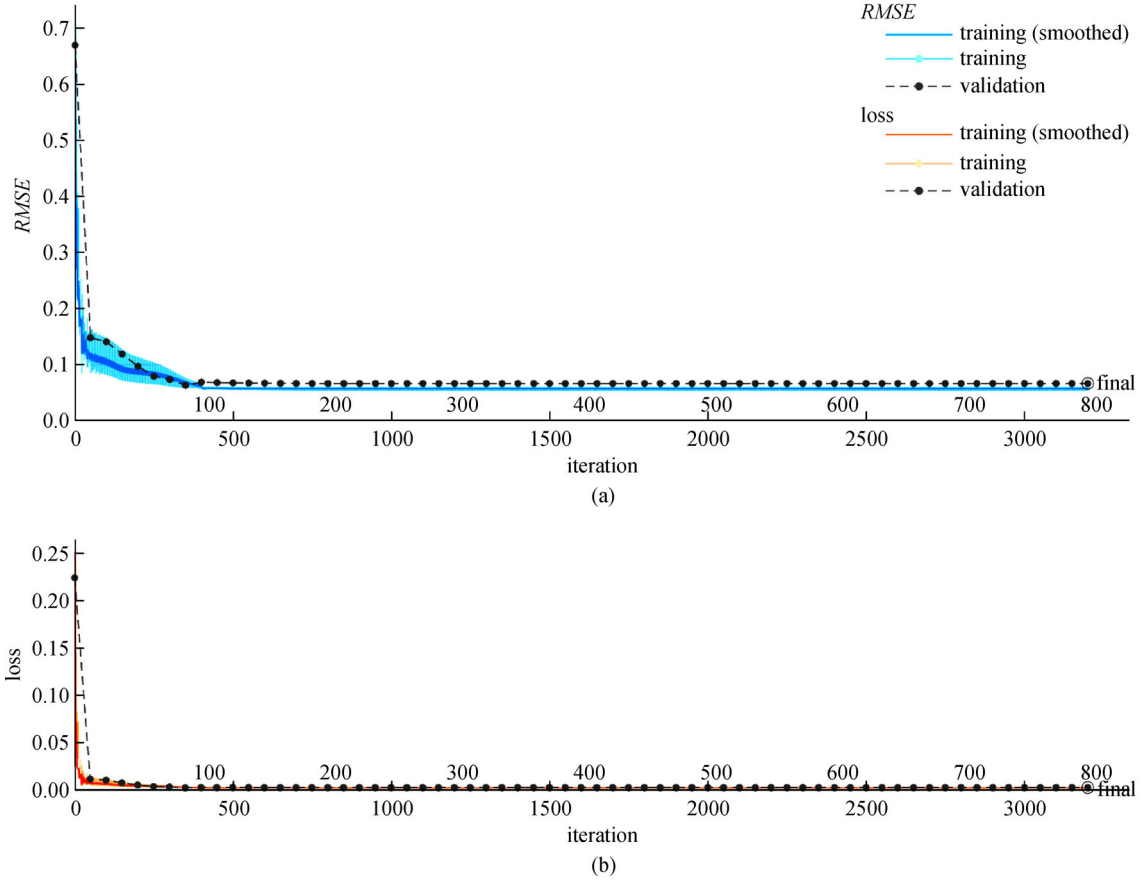

Fig. 22 The training and testing processes of the LSTM network model (third experiment) for UPV. (a) *RMSE*; (b) loss.

methods, were used in this study. The obtained results were evaluated based on various statistical measures. The input data set was divided into training and testing data sets owing to the limited number of samples. Three different division rates were selected as 60% training-40% testing, 70% training-30% testing, and 80% training-20% testing. The results showed that the best prediction performance was obtained from the models used the 80% training-20% testing. In addition, the 70% training-30% testing outperformed the 60% training-40% testing. Moreover, when we compared the performances of the stacked autoencoders and LSTM networks, it was observed that the LSTM network outperformed the stacked autoencoders. The prediction accuracy for the CS and UPV of the LSTM network were found to be 97.60% and 99.24%, respectively. It was also observed that the UPV prediction results were better than the CS prediction results. The LSTM obtained impressive results in the estimation of the CS and UPV of concrete containing silica fume subjected to high temperatures. Furthermore, this study found that LSTM has a very good prediction ability with little experimental data. The predicted results showed that DL has a great potential in civil engineering applications.

Acknowledgements The experimental part of this study was supported by the Firat University BAPYB (Project No. TEF.12.04). The authors gratefully acknowledge the Firat University of BAPYB.

References

1. Schneider U. Concrete at high temperatures—A general review. Fire Safety Journal, 1988, 13(1): 55–68
2. Phan L T. Fire performance of high-strength concrete: A report of the state-of-the art, building and fire research laboratory. Nistir, 1996, 5934: 1–105
3. Poon C S, Azhar S, Anson M, Wong Y L. Performance of metakaolin concrete at elevated temperatures. Cement and Concrete Composites, 2003, 25(1): 83–89
4. Tanyildizi H, Asilturk E. Performance of phosphazene-containing polymer-strengthened concrete after exposure to high temperatures. Journal of Materials in Civil Engineering, 2018, 30(12): 04018329
5. Tanyildizi H, Şahin M. Taguchi optimization approach for the polypropylene fiber reinforced concrete strengthening with polymer after high temperature. Structural and Multidisciplinary Optimization, 2017, 55(2): 529–534
6. Tanyildizi H, Asiltürk E. High temperature resistance of polymer-phosphazene concrete for 365 days. Construction & Building Materials, 2018, 174: 741–748
7. Varona F B, Baeza F J, Bru D, Ivorra S. Influence of high temperature on the mechanical properties of hybrid fibre reinforced normal and high strength concrete. Construction & Building Materials, 2018, 159: 73–82
8. Poon C S, Azhar S, Anson M, Wong Y L. Strength and durability recovery of fire-damaged concrete after post-fire-curing. Cement and Concrete Research, 2001, 31(9): 1307–1318
9. de Oliveira Dias A R, Amancio F A, de Carvalho Rafael M F, Bezerra Cabral A E. Study of propagation of ultrasonic pulses in concrete exposed at high temperatures. Procedia Structural Integrity, 2018, 11: 84–90
10. Haddad R H, Shannis L G. Post-fire behavior of bond between high strength pozzolanic concrete and reinforcing steel. Construction & Building Materials, 2004, 18(6): 425–435
11. Husem M. The effects of high temperature on compressive and flexural strengths of ordinary and high-performance concrete. Fire Safety Journal, 2006, 41(2): 155–163
12. Wu B, Yu Y, Zhao X Y. Residual mechanical properties of compound concrete containing demolished concrete lumps after exposure to high temperatures. Fire Safety Journal, 2019, 105: 62–78
13. Lin W M, Lin T D, Powers-Couche L J. Microstructures of fire-damaged concrete. ACI Materials Journal, 1996, 93: 199–205
14. Arioz O. Effects of elevated temperatures on properties of concrete. Fire Safety Journal, 2007, 42(8): 516–522
15. Anwar Hossain K M. High strength blended cement concrete incorporating volcanic ash: Performance at high temperatures. Cement and Concrete Composites, 2006, 28(6): 535–545
16. Tanyıldızı H. Post-fire behavior of structural lightweight concrete designed by Taguchi method. Construction & Building Materials, 2014, 68: 565–571
17. Tanyildizi H, Coskun A, Somunkiran I. An experimental investigation of bond and compressive strength of concrete with mineral admixtures at high temperatures. Arabian Journal for Science and Engineering, 2008, 33(2): 443–449
18. Biolzi L, Cattaneo S, Rosati G. Evaluating residual properties of thermally damaged concrete. Cement and Concrete Composites, 2008, 30(10): 907–916
19. Schneider U, Diederichs U, Ehm C. Effect of temperature on steel and concrete for PCRV's. Nuclear Engineering and Design, 1982, 67(2): 245–258
20. Ma Q, Guo R, Zhao Z, Lin Z, He K. Mechanical properties of concrete at high temperature—A review. Construction & Building Materials, 2015, 93: 371–383
21. Poon C S, Azhar S, Anson M, Wong Y L. Comparison of the strength and durability performance of normal- and high-strength pozzolanic concretes at elevated temperatures. Cement and Concrete Research, 2001, 31(9): 1291–1300
22. Behnood A, Ziari H. Effects of silica fume addition and water to cement ratio on the properties of high-strength concrete after exposure to high temperatures. Cement and Concrete Composites, 2008, 30(2): 106–112
23. Ni H G, Wang J Z. Prediction of compressive strength of concrete by neural networks. Cement and Concrete Research, 2000, 30(8): 1245–1250
24. Bilim C, Atiş C D, Tanyildizi H, Karahan O. Predicting the compressive strength of ground granulated blast furnace slag concrete using artificial neural network. Advances in Engineering Software, 2009, 40(5): 334–340
25. Topçu I B, Saridemir M. Prediction of compressive strength of concrete containing fly ash using artificial neural networks and fuzzy logic. Computational Materials Science, 2008, 41(3): 305–311
26. Karahan O, Tanyildizi H, Atis C D. An artificial neural network

approach for prediction of long-term strength properties of steel fiber reinforced concrete containing fly ash. Journal of Zhejiang University. Science A, 2008, 9(11): 1514–1523

27. Duan Z H, Kou S C, Poon C S. Prediction of compressive strength of recycled aggregate concrete using artificial neural networks. Construction & Building Materials, 2013, 40: 1200–1206
28. Tanyildizi H. Prediction of the strength properties of carbon fiber-reinforced lightweight concrete exposed to the high temperature using artificial neural network and support vector machine. Advances in Civil Engineering, 2018, 2018: 1–10
29. Sarıdemir M. Prediction of compressive strength of concretes containing metakaolin and silica fume by artificial neural networks. Advances in Engineering Software, 2009, 40(5): 350–355
30. Tanyildizi H. Prediction of compressive strength of lightweight mortar exposed to sulfate attack. Computers and Concrete, 2017, 19(2): 217–226
31. Cha Y J, Choi W, Büyüköztürk O. Deep learning-based crack damage detection using convolutional neural networks. Computer-Aided Civil and Infrastructure Engineering, 2017, 32(5): 361–378
32. Zhang A, Wang K C P, Li B, Yang E, Dai X, Peng Y, Fei Y, Liu Y, Li J Q, Chen C. Automated pixel-level pavement crack detection on 3d asphalt surfaces using a deep-learning network. Computer-Aided Civil and Infrastructure Engineering, 2017, 32(10): 805–819
33. Lin Y Z, Nie Z H, Ma H W. Structural damage detection with automatic feature-extraction through deep learning. Computer-Aided Civil and Infrastructure Engineering, 2017, 32(12): 1025–1046
34. Deng F, He Y, Zhou S, Yu Y, Cheng H, Wu X. Compressive strength prediction of recycled concrete based on deep learning. Construction & Building Materials, 2018, 175: 562–569
35. Anitescu C, Atroshchenko E, Alajlan N, Rabczuk T. Artificial neural network methods for the solution of second order boundary value problems. Computers. Materials & Continua, 2019, 59(1): 345–359
36. Guo H, Zhuang X, Rabczuk T. A deep collocation method for the bending analysis of Kirchhoff plate. Computers, Materials & Continua, 2019, 59(2): 433–456
37. Rabczuk T, Ren H, Zhuang X. A Nonlocal operator method for partial differential equations with application to electromagnetic waveguide problem. Computers, Materials & Continua, 2019, 59(1): 31–55
38. Mohamedbhai G T G. Effect of exposure time and rates of heating and cooling on residual strength of heated concrete. Magazine of Concrete Research, 1986, 38(136): 151–158
39. Chan Y N, Peng G F, Anson M. Residual strength and pore structure of high-strength concrete and normal strength concrete after exposure to high temperatures. Cement and Concrete Composites, 1999, 21(1): 23–27
40. Krizhevsky A, Sutskever I, Hinton G E. ImageNet classification with deep convolutional neural networks. Advances in Neural Information Processing Systems, 2012, 25(2): 1097–1105
41. Hochreiter S, Schmidhuber J. Long short-term memory. Neural Computation, 1997, 9(8): 1735–1780
42. Liu Y, Qin Y, Guo J, Cai C, Wang Y, Jia L. Short-term forecasting of rail transit passenger flow based on long short-term memory neural network. In: 2018 International Conference on Intelligent Rail Transportation. Singapore, 2018, 1–5
43. Gers F A, Schraudolph N N, Schmidhuber J. Learning precise timing with LSTM recurrent networks. Journal of Machine Learning Research, 2003, 3: 115–143
44. Liu G, Bao H, Han B. A stacked autoencoder-based deep neural network for achieving gearbox fault diagnosis. Mathematical Problems in Engineering, 2018, 2018: 1–10
45. Xie J, Zhang Z, Lu Z, Sun M. Coupling effects of silica fume and steel-fiber on the compressive behaviour of recycled aggregate concrete after exposure to elevated temperature. Construction & Building Materials, 2018, 184: 752–764
46. Esen H, Ozgen F, Esen M, Sengur A. Artificial neural network and wavelet neural network approaches for modelling of a solar air heater. Expert Systems with Applications, 2009, 36(8): 11240–11248
47. Esen H, Inalli M, Sengur A, Esen M. Artificial neural networks and adaptive neuro-fuzzy assessments for ground-coupled heat pump system. Energy and Building, 2008, 40(6): 1074–1083